PERGAMON

International Journal of Heat and Mass Transfer 44 (2001) 3095–3102

International Journal of HEAT and MASS TRANSFER

www.elsevier.com/locate/ijhmt

Movement of impingement heat transfer by a single circular jet with a confined wall

Koichi Ichimiya [a,*], Shoichi Takema [b], Shunichi Morimoto [c], Tomoaki Kunugi [d], Norio Akino [e]

[a] *Department of Mechanical System Engineering, Yamanashi University, Takeda-4, Kofu, Yamanashi 400-8511, Japan*
[b] *Imabari Ship building Co., Ltd., Marugame, Kagawa 763-0061, Japan*
[c] *Clarion Co., Ltd., Toda, Saitama 335-0022, Japan*
[d] *Department of Nuclear Engineering, Kyoto University, Sakyoku, Kyoto 606-8501, Japan*
[e] *Japan Atomic Energy Research Institute, Higashiibarakigun, Ooarai, Ibaraki 311-1300, Japan*

Received 2 August 2000; received in revised form 20 October 2000

Abstract

Impingement heat transfer and flow in the radial and circumferential directions by a single circular laminar jet in a flow passage with a confined insulated wall were estimated numerically in a three-dimensional system and were recognized by visualization of a thermosensitive liquid crystal. Local heat transfer is divided into three regions. The first is a two-dimensional forced convection region whose structure is a co-axial circle. The second laminar mixed-convection region begins with the onset of a buoyancy driven flow, which corresponds to thermal plumes rising from the heated impingement surface at discrete circumferential locations. The ascending and descending pair flows form longitudinal streak lines in the mixed convection region. The number of pairs is found to depend on the aspect ratio of circumferential length and distance between nozzle and impingement surface. The third is a three-dimensional natural convection region similar to Benard convection which constructs several cells. The radial Nusselt number distribution averaged along the circumferential direction is also presented corresponding to the flow.

1. Introduction

An impinging jet has been utilized to enhance the heat removal from electrical equipments [1], the temperature equalization of high temperature steel slab [2], the drying of paper sheets and so on. The size of the facility diminishes and the space with a confined wall between the nozzle and the impingement surface is equal to or less than the nozzle diameter. The basic shape of a nozzle is typically a slit-type or circular nozzle. In the case of a slit-type impinging jet with a confined wall, the fluid mean axial velocity does not change in the flow direction after the impingement. On the other hand, in the case of a circular impinging jet with a confined wall, the average velocity decreases in the radial direction because the cross-sectional area increases. Therefore, the local heat transfer and flow are expected to change in the radial and peripheral directions. Factors affecting the heat transfer and flow of a circular impinging jet are entrainment [3–5], cross-flow [6], turbulence [7,8], attitude of the nozzle [9,10] and so on. In previous studies, the distance between the nozzle and the impingement surface was greater than the nozzle diameter, and the local characteristics of heat transfer have not been studied in detail in the radial direction.

In the present study, impingement heat transfer and flow in the radial and peripheral direction by a single circular laminar jet with a confined wall were calculated numerically in a three-dimensional system including the temperature dependency of thermal properties. These

* Corresponding author. Tel.: +81-55 220 8434; fax: +81-55 220 8434.
E-mail address: ichimiya@ccn.yamanashi.ac.jp (K. Ichimiya).

0017-9310/01/$ - see front matter
PII: S0017-9310(00)00341-0

Nomenclature

C_p	specific heat
D	nozzle diameter
g	acceleration of gravity
Gr	Grashof number ($= g\beta(2h)^3(T_w - T_b)/v^2$)
h	space between nozzle and impingement surface
Nu	Nusselt number ($=\alpha D/\lambda$)
p	pressure
q	heat flux
r	coordinate in radial direction
Re	local Reynolds number based on local velocity ($=u2h/v$)
Re_D	Reynolds number at nozzle exit ($=u_m D/v$)
t	time
T	temperature
T_b	bulk fluid temperature
T_w	impingement surface temperature
T_0	fluid temperature at nozzle exit
u	velocity in radial direction
u_m	average velocity at nozzle exit
v	velocity in θ-direction
w	velocity in z-direction
α	local heat transfer coefficient
β	coefficient of thermal expansion
δ	one grid size from the impingement surface
θ	coordinate in peripheral direction
λ	thermal conductivity of fluid
v	kinematic viscosity of fluid
ρ	density of fluid

results were compared with visualization by a thermo-sensitive liquid crystal.

2. Description of the problem

In research on an impinging jet, the jet velocity was essentially high, and the space between nozzle and impingement surface was several times the nozzle diameter. Recently, in practical applications, the jet velocity is not so high, and the space is equal to or less than the nozzle diameter because of the compactness of the facility, the noise, the vibration and so on. In the narrow space, the jet is not decelerated as much and approaches the impingement surface. A single circular impinging jet has been studied in a two-dimensional system and the local three-dimensional characteristics have not been expressed specifically.

In Fig. 1, the coordinate system chosen as the subject of this study is presented. The working fluid is water. The fluid velocity at the nozzle exit has a fully developed laminar distribution. After the fluid impinges on the iso-thermal flat surface, it flows in the radial direction with less velocity across the section. The local heat transfer and flow are estimated numerically in a three-dimensional cylindrical system (r, θ, z) and correspond to the visualization. The dimensions of the system are as follows: the nozzle diameter $D = 20$ mm, the distance between nozzle and impingement surface $h = 10$ mm, the radial distance from the center of the nozzle $r = 300$ mm and the peripheral degree $\theta = 90°$.

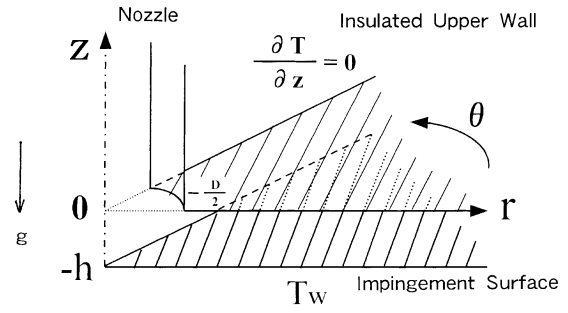

Fig. 1. Coordinate system.

3. Numerical analysis

The three-dimensional governing equations are as follows:

The continuity equation:

$$\frac{\partial ru}{r\partial r} + \frac{\partial v}{r\partial \theta} + \frac{\partial w}{\partial z} = 0. \tag{1}$$

The momentum equations:

$$\begin{aligned}
&\frac{\partial u}{\partial t} + \frac{\partial ruu}{r\partial r} + \frac{\partial vu}{r\partial \theta} + \frac{\partial wu}{\partial z} - \frac{vv}{r} \\
&\quad = \frac{-\partial p}{\rho \partial r} + \frac{\partial r\tau_{rr}}{r\partial r} + \frac{\partial \tau_{\theta r}}{r\partial \theta} + \frac{\partial \tau_{rz}}{\partial z} - \frac{\tau_{\theta\theta}}{r}, \\
&\frac{\partial v}{\partial t} + \frac{\partial ruv}{r\partial r} + \frac{\partial vv}{r\partial \theta} + \frac{\partial wv}{\partial z} - \frac{uv}{r} \\
&\quad = \frac{-\partial p}{\rho r \partial \theta} + \frac{\partial r\tau_{r\theta}}{r\partial r} + \frac{\partial \tau_{\theta\theta}}{r\partial \theta} + \frac{\partial \tau_{z\theta}}{\partial z} - \frac{\tau_{r\theta}}{r}, \\
&\frac{\partial w}{\partial t} + \frac{\partial ruw}{r\partial r} + \frac{\partial uw}{r\partial \theta} + \frac{\partial ww}{\partial z} \\
&\quad = \frac{-\partial p}{\rho \partial z} + \frac{\partial r\tau_{rz}}{r\partial r} + \frac{\partial \tau_{\theta z}}{r\partial \theta} + \frac{\partial \tau_{zz}}{\partial z} - g\beta(T - T_0),
\end{aligned} \tag{2}$$

where Boussinesq approximation is applied to the buoyancy term and

$$\tau_{rr} = 2v\frac{\partial u}{\partial r},$$

$$\tau_{\theta\theta} = 2v\left(\frac{\partial v}{r\partial\theta} + \frac{u}{r}\right),$$

$$\tau_{zz} = 2v\frac{\partial w}{\partial z},$$

$$\tau_{r\theta} = \tau_{\theta r} = v\left(\frac{\partial v}{\partial r} - \frac{v}{r} + \frac{\partial u}{r\partial\theta}\right),$$

$$\tau_{\theta z} = \tau_{z\theta} = v\left(\frac{\partial w}{r\partial\theta} + \frac{\partial v}{\partial z}\right),$$

$$\tau_{zr} = \tau_{rz} = v\left(\frac{\partial u}{\partial z} + \frac{\partial w}{\partial r}\right).$$

The energy equation:

$$C_p\rho\left(\frac{\partial T}{\partial t} + \frac{\partial ruT}{r\partial r} + \frac{\partial vT}{r\partial\theta} + \frac{\partial wT}{\partial z}\right) = \frac{\partial rq_r}{r\partial r} + \frac{\partial q_\theta}{r\partial\theta} + \frac{\partial q_z}{\partial z}, \quad (3)$$

where

$$q_r = \lambda\frac{\partial T}{\partial r}, \quad q_\theta = \lambda\frac{\partial T}{r\partial\theta}, \quad q_z = \lambda\frac{\partial T}{\partial z}.$$

Boundary conditions are as follows. The water temperature and Reynolds number at nozzle exit are $T_0 = 20°C$ and $Re_D = 400$, respectively. The impingement surface temperature is $T_w = 30°C$. The upper wall of the flow passage is insulated thermally. The peripheral gradient of the temperature is zero at $\theta = 0°$ and 90°, and the flow slips there. At the exit of the flow passage, the radial gradients of the velocity and the heat flux are zero.

The computation domain was previously examined for $\theta = 0$–45°, 0–90°, 0–135° and 0–360°. As a result, the characteristics of heat transfer and flow could be evaluated sufficiently in the region of $\theta = 0$–90°. In the temperature region of $T_0 = 20$–30°C, specific heat of the fluid varies 0.12%, the thermal conductivity 1.1% and the kinematic viscosity 21% [11]. Therefore, the specific heat was referred at nozzle exit temperature. The thermal conductivity and kinematic viscosity were approximately expressed by the three-order function of local temperature.

The governing equations were solved by a finite difference method. The SIMPLE algorithm [12] was employed to solve the coupling between the continuity and the momentum equations through pressure. The QUICK scheme was implemented to calculate the convection flux through the cell faces of control volumes. The number of meshes were 150 (r) × 90 (θ) × 10 (z) using staggered grids. The time step 0.007 s was selected for numerical stability.

4. Experimental apparatus of heat transfer visualization and procedure

A schematic diagram of the experimental apparatus of heat transfer visualization on the impingement surface is shown in Fig. 2. The temperature of the working fluid (water) was controlled within 0.05°C by a constant temperature water bath. The water was carried to a circular nozzle via a flow meter, and the flow rate was controlled by a bypass. The circular nozzle made of transparent acrylic resin tube had a developing section with a 20-mm inner diameter and 1000-mm length. The space between the nozzle and the impingement surface was 10 mm. The heated section made of aluminum had a 330-mm outer diameter and was 15-mm thick. A rubber heater (maximum heat flux 2 W/cm^2) was equipped to the rear in the section. The thermal diffusivity of aluminum is very high, and its surface temperature is almost uniform. This was confirmed by seven thermocouples located 1 mm depth along radial direction. The thermosensitive liquid crystal sheet placed on the surface of aluminum was 310-mm long and 220-mm wide. The structure of the liquid crystal layer is shown in Fig. 3 [13]. "PET" is a transparent thermoresistant layer which protects the liquid crystal layer. "Black" is a dye to darken the background so as to allow observation of the scattered light from the liquid crystal. The temperature difference was generated by producing a thin thermoresistant layer between the constant temperature surface and liquid crystal layer. This local temperature differ-

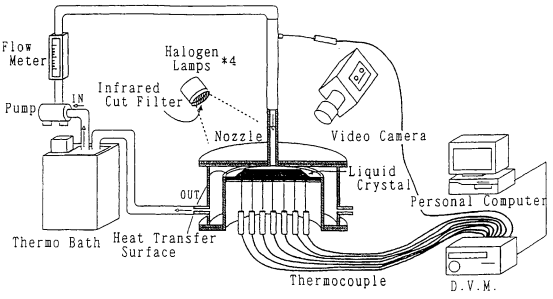

Fig. 2. Experimental apparatus.

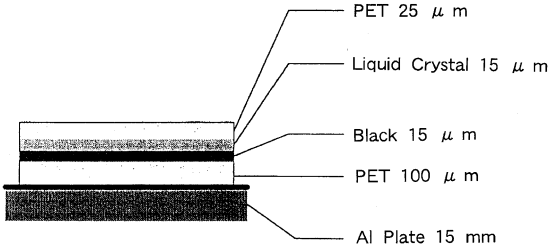

Fig. 3. Structure of thermosensitive liquid crystal layer.

ence corresponds to the local heat flux. The liquid crystal used was a kiral-nematic type, and the sensitive temperature range was from 28°C (red) to 34°C (blue). Four halogen lamps with infrared cut filters were placed at a height of 400 mm and an angle of 45° in relation to the impingement surface for the illumination. After the water flow rate was controlled, the rubber heater was heated electrically. Heat transfer on the impingement surface was visualized in the steady condition, and pictures were taken. The flow was also visualized by injecting a dye.

5. Results and discussions

In Fig. 4, the numerical results of temperature distribution at one-mesh from the impingement surface are presented. The temperature is expressed in the following equation:

$$T = T_w - (q\delta/\lambda), \tag{4}$$

where δ is one mesh size. Local temperature T corresponds to the local heat flux q because of the constant impingement surface temperature ($T_w = 30$°C). The coordinate $(0,0)$ corresponds to the center of the circular nozzle. After the impingement of the fluid, the flow changes to the radial direction. The heat flux distribution is co-axial and two-dimensional from $r = 0$ mm to $r \fallingdotseq 40$ mm and is dominated by forced convection. After that, the wide and narrow streak lines with dark blue and pink colors are generated peripherally and alternatively to $r \fallingdotseq 140$ mm. This indicates a three-dimensional mixed convection with rising and falling flow by forced and natural convection. To the downstream region from $r \fallingdotseq 150$ mm, cell constructions such as a Benard convection are generated.

Heat flux visualization corresponding to the numerical results is shown in Fig. 5. The color distribution of the liquid crystal corresponds to the local heat flux distribution. Beneath the nozzle, the color is red, and the local heat flux is high. From $r = 0$ mm to $r \fallingdotseq 40$ mm, the color changes coaxially from brown, yellow, yellow–green to green. After $r \fallingdotseq 50$ mm, alternate streak lines of green and orange are generated peripherally and expand in the radial direction. These two-dimensional forced convection and three-dimensional mixed convection regions agree well with the numerical results.

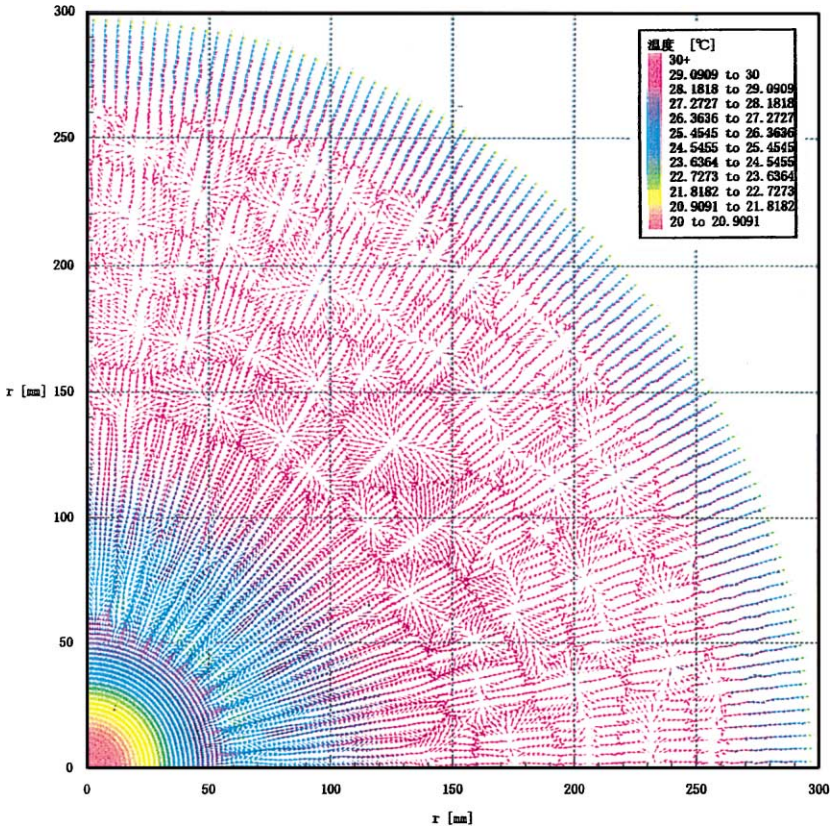

Fig. 4. Temperature and flow behavior.

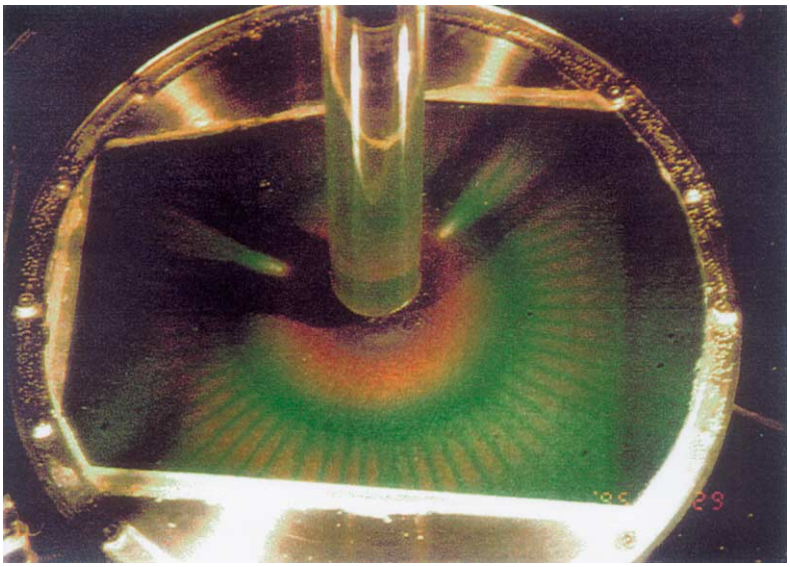

Fig. 5. Heat flux visualization by liquid crystal.

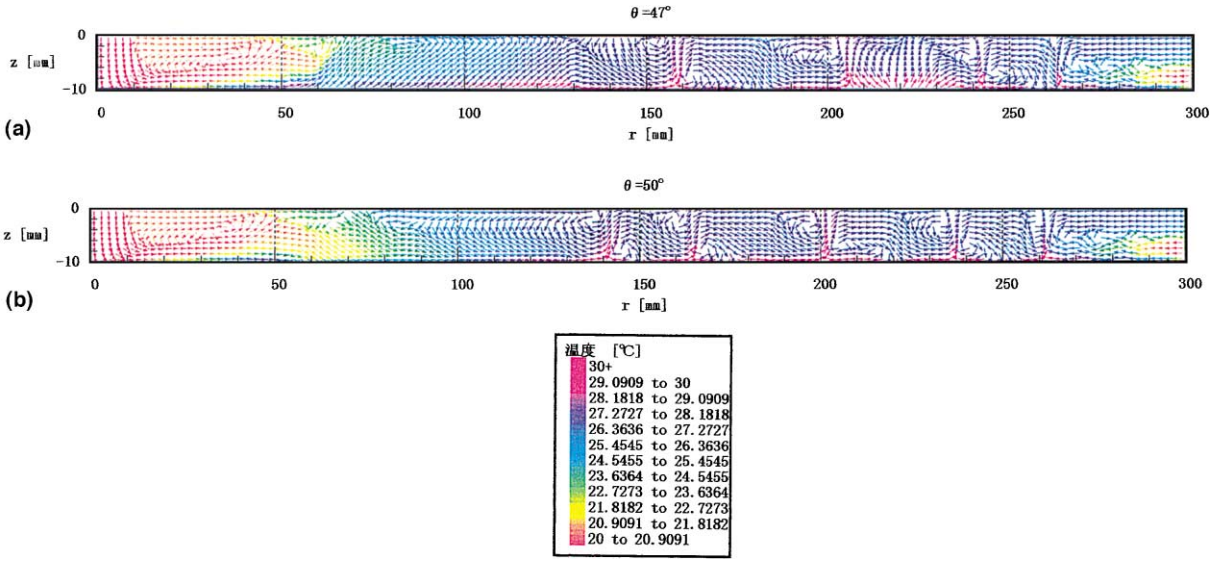

Fig. 6. Temperature and flow behavior along radial direction.

Figs. 6(a) and (b) show the radial temperature distribution (color distribution) and velocity vectors (arrows) relative to Fig. 4. "$r = 0$" denotes "beneath the center of the nozzle", and the radial length scale is compressed to two-thirds of the z-direction. In Fig. 6(a) ($\theta = 47°$), a counterclockwise recirculated flow is generated in the region of $r = 0$ to $r \fallingdotseq 40$ mm on the upper insulated wall. In the region of $r = 60$–130 mm, the flow rises up, after which small recirculated flows can be found with alternate rising and falling flows. On the other hand, in Fig. 6(b) ($\theta = 50°$), the flow falls down in the region of $r \fallingdotseq 60$ mm to $r \fallingdotseq 130$ mm. Therefore, both figures (Figs. 6(a) and (b)) present that the flow changes periodically in the peripheral direction. The peripheral distributions of temperature and velocity vectors are presented in Fig. 7. Peripheral flow does not exist at $r \fallingdotseq 40$ mm, but is generated near the impingement surface at $r \fallingdotseq 50$ mm. The rising blue flow and the falling yellow–green or orange flow are constructed across the whole section at $r \fallingdotseq 60$ mm. These rising and falling flows correspond to the narrow and wide streak lines in Fig. 5, respectively. The number of pairings of rising and

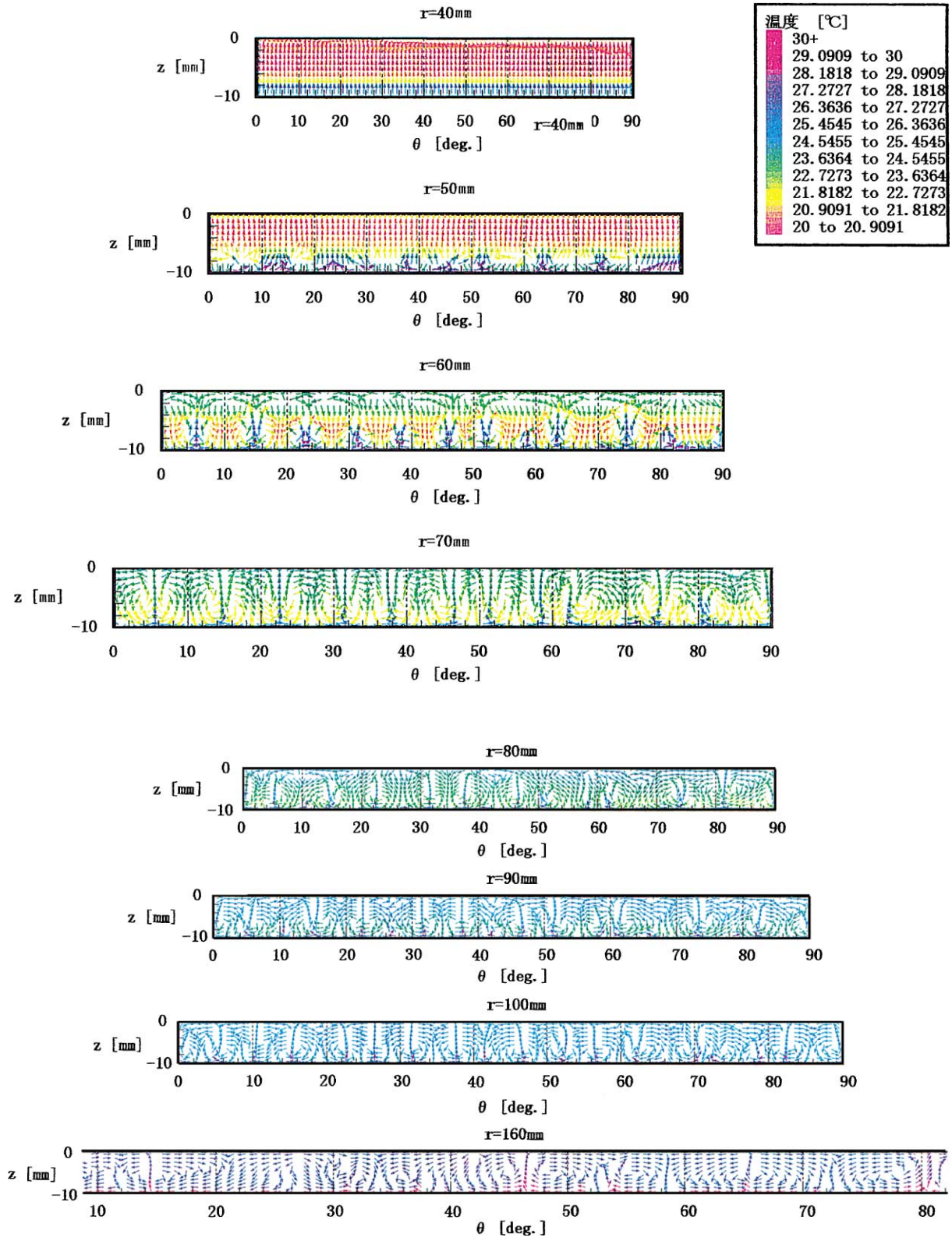

Fig. 7. Temperature and flow behavior along circumferential direction.

falling flows, where the mixed convection starts, depends on the aspect ratio of the peripheral distance to the space between nozzle and impingement surface. In the downflow region of $r \fallingdotseq 70$ mm, a rising flow impinges directly on the insulated upper wall. This indicates the existence of a three-dimensional mixed flow. The streak lines of the mixed flow are the same as the phenomena which Incropera et al. [14] observed as a mushroom-shaped recirculated flow formed by a pair of rising and falling flows across the width of a horizontal rectangular duct in the transition region from the forced convection to the mixed flow. The average velocity across the section is constant due to the rectangular duct. In the present study, the velocity reduction along the radial direction strongly induces the buoyancy force. Therefore, the downward flow region from $r \fallingdotseq 150$ mm is dominated by natural convection with the top insulated and the bottom heated, and the flow moves to the Benard cell. The peripheral flow typically dominates at $r = 160$ mm, and a cell with a rising and falling flow is constructed. The local intensity ratio of natural convection to forced convection, Gr/Re^2, is presented in Fig. 8. The characteristic length of local Reynolds number Re and local Grashof number, Gr is $2h$ because the flow passage with confined wall after impingement has the height of $2h$. The onset of the mixed flow occurs at $Gr/Re^2 = 80$–100, which is almost consistent with $Gr/Re^2 = 65$–150 obtained by Incropera et al. [14]. The flow moves to Benard convection at $Gr/Re^2 = 400$–500.

Radial distribution of the peripherally averaged Nusselt number is displayed in Fig. 9 to examine the heat transfer. The Nusselt number takes the minimum because of the bouncing phenomenon and a small recirculated flow near the impingement surface from $r = 40$ mm to $r = 60$ mm. It peaks at the reattached region of the main flow in Fig. 6. The Nusselt number increases at $r \fallingdotseq 200$ mm because the local heat flux rises due to the backflow from the exit in Fig. 4. The temperature dependency of the thermal conductivity and kinematic viscosity of the fluid appears in the deviation

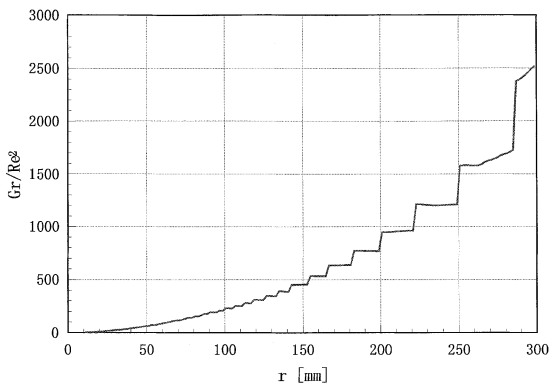

Fig. 8. Gr/Re^2 along radial direction.

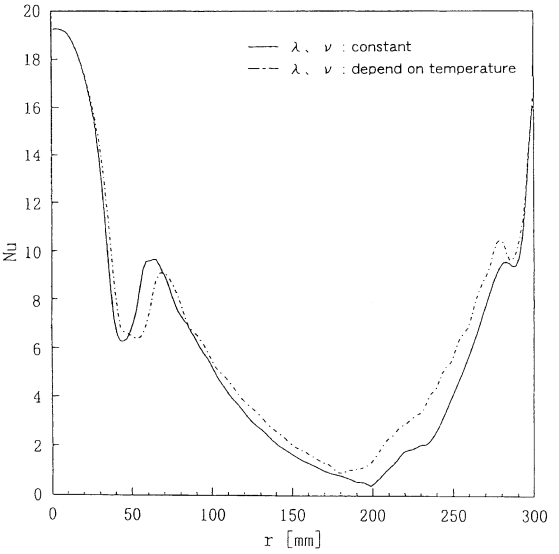

Fig. 9. Nusselt number along radial direction.

from the position of the maximum Nusselt number. As the kinematic viscosity of water becomes low at high temperature and the viscous diffusion also decreases, a small recirculated flow is generated at the downward-flow region relative to the result for constant thermal properties based on the nozzle exit temperature T_0. Therefore, the positions of the maximum and minimum Nusselt numbers move to the downward-flow region (chain line in Fig. 9). Near the exit, the position of the minimum Nusselt number ($r \fallingdotseq 200$ mm) moves to the upward region due to the backflow.

6. Conclusions

The peripheral and radial characteristics of the heat transfer and flow of a single circular impinging jet on an isothermal flat surface were examined by numerical calculation and experimental visualization. After the impingement, the flow was classified into three regions, namely, the two-dimensional forced convection region, the three-dimensional mixed convection region and the natural convection region. In the mixed convection region, the rising and falling flows were generated alternately along the peripheral direction and were recognized by streak lines. The mixed convection was kept in the region of $Gr/Re^2 = 80$–500. In the natural convection region, cells such as Benard convection were formed as the local recirculated flow.

References

[1] B.R. Hollworth, M. Durbin, Impingement cooling of electronics, ASME J. Heat Transfer 114 (1992) 607–613.

[2] K. Ichimiya, K. Kobayashi, R. Echigo, Fundamental study on the flattening of temperature distribution of a high temperature steel slab (part 1, impingement heat transfer and flow situation around a heated slab caused by a laminar slot jet), Trans. JSME 52/474 (1986) 904–909.
[3] B.R. Hollworth, L.R. Gero, Entrainments effects on impingement heat transfer (part 2, local heat transfer measurements), ASME J. Heat Transfer 107 (1985) 910–915.
[4] J.W. Baughn, A.E. Hechanova, Y. Xiaojun, An experimental study of entrainment effects on the heat transfer from a flat surface to a heated circular impinging jet, in: Proceedings of the ASME/JSME Thermal Engineering Joint Conference, Reno, USA, 1991, pp. 17–22.
[5] C.O. Popiel, O. Trass, Visualization of a free and impinging round jet, Exp. Thermal Fluid Sci. 4 (1991) 253–264.
[6] R.J. Goldstein, A.I. Behbahani, Impingement of a circular jet with and without cross-flow, Int. J. Heat Mass Transfer 25 (1982) 1377–1382.
[7] J. Tso, F. Hussain, Organized motions in a fully developed turbulent axisymmetric jet, J. Fluid Mech. 203 (1989) 425–448.
[8] K. Ichimiya, Heat transfer and flow characteristics of a single circular impinging jet considered on heat conduction in a heated section, in: K. Hanjalic, J.C.F. Pereira (Eds.), Turbulence Heat and Mass Transfer, vol. 1, 1995, pp. 258–263.
[9] R.J. Goldstein, M.E. Franchett, Heat transfer from a flat surface to an oblique jet, ASME J. Heat Transfer 110 (1988) 87–93.
[10] K. Ichimiya, Heat transfer and flow characteristics of an oblique turbulent impinging jet within confined walls, ASME J. Heat Transfer 117 (1995) 316–322.
[11] JSME (Ed.), Thermal Properties of Fluids, JSME, Tokyo, 1983, pp. 208–209.
[12] S.V. Patankar, Numerical Heat Transfer and Fluid Flow, Hemisphere, London, 1980, pp. 113–134.
[13] N. Akino, S. Kubo, Heat flux visualization using liquid crystal sheet, in: Proceedings of the 23rd Symposium Visualization Society, Japan, 1995, pp. 67–70.
[14] F.P. Incropera, A.L. Knox, J.R. Maughan, Mixed convection flow and heat transfer in the entry region of a horizontal rectangular duct, ASME J. Heat Transfer 109 (1987) 434–439.